

# 1 Performance of an acoustic sensing array in 2 a high-flow tidal channel

3 Matthew Auvinen, David Barclay

4 **Abstract**

5 Baseline ambient sound level assessment is important in quantifying noise contributions from tidal energy  
6 infrastructure. Static acoustic sensing in high-flow conditions is complicated by pseudo-sound, or flow noise,  
7 generated by pressure fluctuations due to turbulent flow on the surface of a hydrophone. Signal processing methods  
8 are used to identify and suppress flow noise at low frequencies. A four-element horizontal hydrophone array using  
9 data collected in the Minas Passage in the Bay of Fundy in October, 2016. Spectral slope and spatial coherence  
10 are used to track the masking effect of turbulence across frequency and flow speed, and identify the spectral  
11 and coherence critical frequencies. The array's performance in the Minas passage is quantified by an empirical  
12 relationship between flow speed and the spectral critical frequency of a coherent linear array. Beamforming is  
13 proposed as a possible flow noise suppression method and evaluated.

14 **Index Terms**

15 Flow noise, ambient noise, acoustical array, tidal channel, and passive acoustic monitoring.

16 **I. INTRODUCTION**

17 **T**IDAL power utilities are currently leasing seafloor space within the Minas Passage in the Bay  
18 of Fundy with aspirations of converting the energy of the region's tidal currents into electricity,  
19 a trend that has been supported by favorable projections of the Passage's tidal energy capacity [1]. As  
20 these companies seek sector development, it is important that they maintain sustainable industry practices.  
21 This includes the consideration of industry knowledge gaps, many of which are a consequence of the  
22 sector's immaturity [2]. The uncertainty surrounding the ecological and environmental implications of

Matthew Auvinen is a former honours student of David Barclay's in the Department of Oceanography, Dalhousie University, Halifax NS, B3H4R2 Canada (email:matthewauvinen@gmail.com; DBarclay@Dal.Ca).

Manuscript received July XX, 2017; revised MONTH XX, 201X. This work was supported by GeoSpectrum, Black Rock Tidal Power, and the National Sciences and Engineering Research Council of Canada

23 tidal turbine infrastructure is a particularly important knowledge gap and has qualified some opposition  
24 to turbine projects.

25 Tidal turbines present two serious environmental threats: physical contact (or interaction) with marine  
26 life [3] [4] and acoustic pollution.

27 Tidal turbines could become an important source of ambient noise in tidal channels through cavitation  
28 and motor or mechanical noise [5]. Turbine anthropophony could affect animal navigation, communication,  
29 predator-prey detections [6], and marine life cycles [7]. Moreover, turbine-generated sound could be  
30 damaging to fish tissue [8]. These acoustic effects threaten near-field and far-field ecosystem health,  
31 stressing the need for rigorous environmental impact assessments in the tidal power sector.

32 As a result, tidal power companies are interested in establishing baseline ambient noise measurements  
33 in the Minas Passage, against which turbine noise pollution will be measured. However, the utility of  
34 ambient sensing is limited by pseudo-sound, or flow noise, generated on the surface of a hydrophone  
35 in turbulent water. Indeed, the masking effects of flow noise can complicate source identification and  
36 background noise assessment in high-flow settings, such as tidal channels.

37 Analogous to the turbulent air flow pseudo-sound described in [9], flowing water in a high Reynolds  
38 number regime generates pressure fluctuations on the surface of a hydrophone. These pressure fluctuations  
39 produce flow noise which is irregular, uncorrelated, and random. Local pressure fluctuations on the surface  
40 of a hydrophone represent near-field turbulence [10]. Hydrophones moving with the mean water flow will  
41 experience little signal contamination, as it is the relative flow of water over a hydrophone's surface that  
42 leads to flow noise.

43 Turbulent flows occupy a wide range of frequencies and wavenumber domains, with broad spatial and  
44 temporal variability. The advective nonlinearity of turbulent flows makes them unpredictable in space and  
45 time, and contributes to their complex nature [11]. Despite being governed by classical mechanics and  
46 cascade laws, turbulence and its corresponding flow noise are difficult to predict.

47 The degree of variability within turbulence (and flow noise) makes it difficult to reliably model flow  
48 noise characteristics. Identifies steep spectral slopes in a high-flow setting, an artifact of small-scale  
49 turbulence averaged out across the surface of a submerged sensor. This slope,  $f^{-m}$ , is modeled and  
50 described in [2]. Furthermore, a spectral slope of  $f^{-5/3}$  - not to be confused with the coincidental wind-  
51 generated spectral slope, which occurs at higher frequencies [13] - has been reported at frequencies below  
52 at frequencies below 20 Hz [12].

53 Flow noise presents a unique challenge for passive acoustic monitoring (PAM): a hydrophone in  
54 a high-flow setting will record both propagating sound and pseudo-sound. This suggests that models  
55 should distinguish between the two sound sources in order to properly evaluate ambient signals.]  
56 describes the exploitation of uncorrelated flow noise to suppress pseudo-sound in deep ocean ambient  
57 noise measurements.

58 Successful suppression of flow noise could benefit PAM systems in the tidal energy sector. The objectives  
59 of the present research are:

- 60 1) Use spectral analysis and spatial coherence to identify and characterize flow noise at low frequencies  
61 ( $< 500$  Hz).
- 62 2) Use coherent averaging (beamforming) to improve the performance of a linear hydrophone array  
63 by suppressing flow noise and enhancing the measurement of ambient noise.

64 This paper is organized as follows. Section II discusses important field work details, including site  
65 description and instrumentation. Section III contains all relevant signal processing, emphasizing spectral  
66 analysis, spatial coherence, and beamforming. Section IV presents the signal processing and data analysis  
67 results. Section V evaluates the results and identifies areas for future work. Lastly, Section VI summarizes  
68 the findings of the study in a series of conclusions.

## 69 II. FIELD WORK

70 Field work was completed on October 27, 2016, near the Fundy Ocean Research Center for Energy  
71 (FORCE) site in the Minas Passage of the Bay of Fundy. The deployment period spanned roughly four  
72 hours, from 12:00 ADT to 16:00 ADT. This experimental window captured the transition from ebb tide  
73 to slack tide.

74 Wind speed was measured intermittently throughout the deployment period using a hand-held wind  
75 speed gauge (Table I) and tidal data was generated using the Web models.

TABLE I  
WIND SPEED MEASUREMENTS TAKEN OVER THE DEPLOYMENT PERIOD.

Time (ADT)	Wind speed (m/s)
13:35	4.9
14:35	5.2
15:00	6.2
15:10	6.2
15:35	4.2
15:48	3.2

### 76 A. Experiment

77 A linear hydrophone array was streamed behind the *MV Nova Endeavour* (42' x 16'), which was  
 78 anchored to the seafloor in the Minas Passage. The array was positioned 15 meters below the sea surface  
 79 using a depressor. Four hydrophones were simultaneously sampled over a four hour period and processed  
 80 by an analog-to-digital converter (ADC) on board the *MV Nova Endeavour*. The signal cable, which  
 81 carried both the array and a drogue, was sheathed in a fairing to reduce strum generation and attached to  
 82 a tow cable (6GA galvanized wire) using cable ties.

83 A drifting hydrophone (Geospectrum Technologies GuardBuoy) was deployed using a small auxiliary  
 84 vessel launched from the *MV Nova Endeavour*. The GuardBuoy was suspended 2 meters below the surface  
 85 using a drifting surface float and isolation system made of spectra and compliant bungee. The system  
 86 isolated the recording hydrophone and instrument package from any surface action, such as the vertical  
 87 movement of waves, which would otherwise generate mechanical or flow noise.

88 A total of five transects were performed by driving the guard buoy upstream, deploying the drifter, then  
 89 floating downstream in a rigid-hulled inflatable boat (RHIB) alongside the Guard Buoy until both had  
 90 reached 50 feet past the array. These transects were performed over the course of three hours, beginning  
 91 at 13:00 ADT. The Guard Buoy signals are assumed to be flow noise free and were used as benchmarks  
 92 to assess the performance of the array.

### 93 B. Instrumentation

94 The linear array was constructed by GeoSpectr<sup>®</sup> and contains four sequentially spaced hydrophones  
 95 with a horizontal configuration (Fig. 1). Each hydrophone pair is separated by a distance  $d = 17\text{cm}$ . The

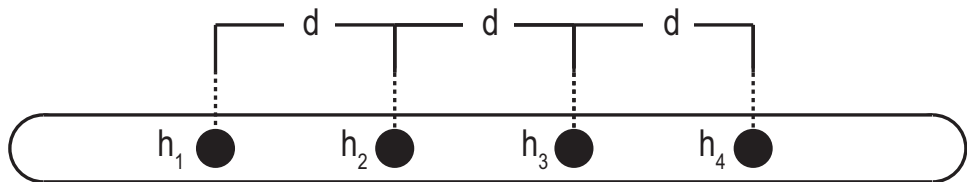


Fig. 1. Schematic view [§]ear array. Hydrophones,  $h$ , and the separation distance,  $d$ , are labelled.

array hydrophones were set t[§]imple at a rate of 96.038 kHz with an acoustic bandwidth of 48.019 kHz. The four channels on the array continuously recorded 10 minute WAV files over a 4 hour period. Power spectra were calibrated to dB re 1  $\mu$ Pa according to frequency-dependent sensitivities supplied by the manufacturer. The GuardBuoy sampled at a rate of 96 kHz with an acoustic bandwidth of 48 kHz, and was equipped with a GPS to record transect geospatial information. The Guard Buoy recorded WAV files in 30 minute segments ~~and saved them to its 2 GB hard drive~~. Corresponding power spectra were converted to dB re 1  $\mu$ Pa according to frequency-dependent sensitivities supplied by the manufacturer.

103

### III. DATA ANALYSIS

Data analysis was performed in MATLAB in several stages. The analysis began with the calculation of the power spectral density (PSD) from the raw WAV files, followed by spectral analysis, spatial coherence, and beamforming.

107 *A. General Signal Processing*

The output of a hydrophone is defined as

$$x_i(t) = \sigma_i(t) + n_i(t) \quad (1)$$

where  $x_i$  is the recorded time series on each  $i$ th hydrophone,  $\sigma_i$  is the sound field's ambient components, and  $n_i$  is the locally generated flow noise. Importantly,  $n_i$  and  $\sigma_i$  are uncorrelated. Furthermore, the inherent randomness of flow noise makes  $n_i$  incoherent with respect to  $n_j$ .

The power spectrum, or spectral density, is defined as

$$S_{ii}(\omega) = \frac{\langle X_i(\omega) \cdot X_i^*(\omega) \rangle}{T} \quad (2)$$

111 where  $X_i$  is the Fourier transform of  $x_i$ ,  $\omega$  is angular frequency,  $*$  denotes a complex conjugate,  $\langle \rangle$   
 112 indicates an ensemble average, and  $T$  is the observation interval. All Fourier transforms are windowed  
 113 by a Hann function. The Fourier transform is  $2^{16}$  points long and contains 99 degrees of freedom.

Coherence is used to quantify the similarity between two signals. ~~Here, coherence is~~ defined as

$$\Gamma_{ij}(\omega) = \frac{S_{ij}(\omega)}{(S_{ii}(\omega) \cdot S_{jj}(\omega))^{\frac{1}{2}}}. \quad (3)$$

114 **B. Power Spectrum Probability Density**

115 Spectral probability density (SPD) is an analytical technique used to depict the variability of the power  
 116 spectrum over a period that is much longer than the minimum time required for a stationary measurement  
 117 of power to be made [15]. This form of analysis facilitates the identification of unique events within a  
 118 series of spectra.

The power spectrum probability density (PSPD) is defined as

$$\text{PSPD}(f) = H(S_{ii}(f), h) \quad (4)$$

119 where  $\text{PSPD}(f)$  is the power spectrum probability density at frequency  $f$ , and  $H(S(f), h)$  is the histogram  
 120 of the power spectrum  $S_{ii}$  at frequency  $f$  with a histogram bin width of  $h$  dB re 1  $\mu\text{Pa}$ . By combining  
 121 PSPD results across frequencies, we generate a PSPD matrix

$$\begin{bmatrix} \text{PSPD}(f_1) & \text{PSPD}(f_2) & \text{PSPD}(f_3) & \dots & \text{PSPD}(f_a) \end{bmatrix} \quad (5)$$

122 where  $\text{PSPD}(f_a)$  is the PSPD at the  $a$ th frequency.

123 **C. Spectral Critical Frequency**

124 [6] [12] suggest that there are three distinct spectral slope regions in the low-to-mid-frequency  
 125 range: Kolmogorov's  $f^{-5/3}$  spectral slope; steepened flow noise spectral slopes of  $f^{-m}$  [12]; and an  
 126 ambient noise region that is determined by near-field and far-field ambient sound sources.

Spectral type is defined as

$$f^{-M} = \frac{S_{ii}(2\pi f_a) - S_{ii}(2\pi f_b)}{\log(f_a \cdot f_b^{-1})} \quad (6)$$

127 where  $S_{ii}(2\pi f_a)$  is the spectral density on the  $i$ th sensor at frequency  $f_a$  and  $S_{ii}(2\pi f_b)$  is the spectral  
 128 density on the  $i$ th sensor at frequency  $f_b$ . (6) describes the spectral slope in dB/decade.  $f^{-m}$  from [12] is  
 129 found using (6).

The transition from the flow noise region of  $f^{-m}$  to the ambient noise region is marked by the ‘frequency knee’, where the spectral slope begins to shallow. That is, the exit from the flow noise region is marked by a deviation below the slope  $f^{-m}$ . Here, critical frequency,  $f_c$ , is defined as the first frequency at which

$$|f^{-M}| < |f^{-m}| \quad (7)$$

130 is true. Importantly, both slopes in (7) are in dB/decade. This form of analysis produces the spectral  
 131 critical frequency,  $f_c$ .

#### 132 D. Coherence Critical Frequency

133 Spatial coherence is calculated for each channel combination using (3), providing an assessment of  
 134 signal similarity between elements. Propagating ambient noise is highly correlated across the array.  
 135 Additionally, propagating noise at wavelengths sufficiently large relative to element spacing produces  
 136 very high coherence at low frequencies by effectively co-locating sensors. Conversely, flow noise is a  
 137 source of incoherence, as pseudo-sound is uncorrelated across the linear array (when turbulent scales are  
 138 lesser than hydrophone separation). Therefore, in the band  $f < 500$  Hz, flow noise is marked by low  
 139 coherence while ambient noise is marked by high coherence. The transit of this coherence boundary, from  
 140 flow noise (incoherent) to ambient noise (coherent) provides a metric for describing the extent of flow  
 141 noise across the array.

The spatial coherence critical frequency,  $f'_c$ , is defined as the frequency at which a minimum coherence threshold is crossed. To establish this coherence threshold, we assume an isotropic ambient field such that the coherence over the 0–500 Hz frequency band is estimated with

$$G_{ij} = \frac{\sin w'}{w'} \quad (8)$$

where

$$w' = \frac{2\pi d \cdot c}{c} \text{ Hz} \quad (9)$$

Here  $\text{hydrophone}$  is the hydrophone separation distance and  $c$  is the local sound speed. Formally,  $f'_c$  is the first frequency at which

$$|\Gamma_{ij}(\omega)| \leq 0.9 \cdot G_{ij} \quad (10)$$

is true. We can be confident that any coherence within 10% of (8) is real and significant. This automated critical frequency detector corresponds to coherence thresholds between 0.7 - 0.9 depending on the hydrophone separation distance.

#### 145 E. Linear Regression

146 A linear regression between critical frequencies,  $f_c$  and  $f'_c$ , and flow speed,  $u$ , is used to identify and  
 147 characterize the prevalence of flow noise and ambient noise in measurements. Importantly, no data points  
 148 are excluded from this regression.

#### 149 F. Beamforming

We use a broadside beamformer to coherently average the channels across the array. Locally generated flow noise and the ambient sound field are inseparable, however we can describe their relative prevalence with the theoretical signal-noise ratio (SNR). By taking the Fourier transform of (1) and substituting into (2), we find

$$S_{ii} = \frac{\langle (\zeta_i + N_i) \cdot (\zeta_i^* + N_i^*) \rangle}{T} \quad (11)$$

where  $\zeta_i$  and  $N_i$  are the Fourier transforms of  $\sigma_i$  and  $n_i$ , respectively. For clarity, the frequency dependency has been omitted. Since  $\zeta_i$  and  $N_i$  are uncorrelated, we can expand (11) to arrive at

$$S_{ii} = \frac{\langle \zeta_i \zeta_i^* \rangle + \langle N_i N_i^* \rangle}{T}. \quad (12)$$

Given (12), the SNR for a single hydrophone ( $\text{SNR}_H$ ) is defined as

$$\text{SNR}_H = \frac{\langle \zeta_i \zeta_i^* \rangle}{\langle N_i N_i^* \rangle} \quad (13)$$

where  $\text{SNR}_H = 1$  at the critical frequency,  $f_c$ . Now consider an array of hydrophones indexed by  $i$ , where the ambient sound field component of the signal on each phone is

$$\sigma_{i+1}(t) = \sigma_1(t - \tau_i) \quad (i > 1) \quad (14)$$

where

$$\tau_i = \frac{i \cdot d \cos \theta}{c} \quad (15)$$

is the acoustic travel time in seconds for plane wave noise arriving on the sensors at the angle  $\theta$ . Here,  $d$  is the nearest neighbour element separation (Fig. 1). Taking the Fourier transform of (14) gives

$$\varsigma_i(\omega) = \varsigma_1(\omega) e^{-i\omega\tau_i}. \quad (16)$$

The coherent sum of the signals ~~on each element~~ is defined as

$$x_T(t) = \sum_{i=1}^l x_i(t) \quad (17)$$

where  $x_i(t)$  is the signal recorded on the  $i$ th element of a linear array  $l$  elements long. Since no time delay has been applied to  $x_i(t)$ ,  $x_T(t)$  is the equivalent to beamforming broadside to the array. Since the source of interest is ambient noise, the sound field is assumed to be axially symmetric. Thus the horizontal array orientation and beam direction are unimportant, provided an appropriate array gain compensation is applied. The Fourier transform of (17) is

$$X_T(\omega) = \sum_{i=1}^l X_i(\omega). \quad (18)$$

The array power spectral density can be estimated using (18) by

$$A = \frac{\langle X_T(\omega) \cdot X_T^*(\omega) \rangle}{T}. \quad (19)$$

Given an array with both ambient noise and flow noise components, (18) can be expanded to

$$X_T = [\varsigma_1 + N_1 + \varsigma_2 + N_2 + \dots + \varsigma_l + N_l] \quad (20)$$

which describes the total output of all sensors on an array with  $l$  elements. Substituting (16) into (20) gives

$$X_T = \varsigma_1 + N_1 + \sum_{i=1}^l (\varsigma_1 e^{-i\omega\tau_i} + N_{i+1}). \quad (21)$$

Using the Fourier transform of the coherently summed outputs across the array, the power spectral density can be computed by substituting (21) into (19) yielding

$$A = \frac{\langle \varsigma_1 \varsigma_1^* \left[ l + \sum_{i=1}^{l-1} \frac{1}{2} (l-i) \cos(\omega\tau_i) \right] + N \cdot N^* \rangle}{T} \quad (22)$$

where

$$N = \sum_i^l N_i \quad (23)$$

is the coherently summed flow noise. This term can be simplified by assuming the power of the flow noise measured on each individual hydrophone is equal across the array,

$$\langle N_i N_i^* \rangle = \langle N_j N_j^* \rangle \quad (24)$$

and uncorrelated between the sensors,

$$\langle N_i N_j^* \rangle = \delta_{ij} \cdot N_1 N_1^* \quad (25)$$

150

$$\delta_{ij} = \begin{cases} 0 & \text{if } i \neq j \\ 1 & \text{if } i = j. \end{cases}$$

Then the total power received by the array becomes

$$A = \frac{\langle \varsigma_1 \varsigma_1^* \rangle \left[ l + \sum_{i=1}^{l-1} \frac{1}{2} (l-i) \cos(\omega\tau_i) \right] + l \langle N_1 N_1^* \rangle}{T}. \quad (26)$$

Furthermore, if  $K$  is defined as

$$K = l + \sum_{i=1}^{l-1} \frac{1}{2} (l-i) \cos(\omega\tau_i) \quad (27)$$

then (26) becomes

$$A = \frac{K\langle \zeta_1 \zeta_1^* \rangle + l\langle N_1 N_1^* \rangle}{T} \quad (28)$$

where (28) describes the array spectral density. Here,  $SNR_A$  describes the relative strength of the ambient noise and flow noise components of the array output, such that

$$SNR_A = \frac{K\langle \zeta_1 \zeta_1^* \rangle}{l\langle N_1 N_1^* \rangle}. \quad (29)$$

Comparing (29) to the result derived for a single hydrophone, given by (13), we see that the beamformed array improves the signal-to-noise ratio by a factor of  $\frac{K}{l}$ . Furthermore, (29) suggests that array performance improves with an increasing number of hydrophones,  $l$ . For an array with 4 elements, at broadside,  $\frac{K}{l} = \frac{7}{4}$ .

### 155 G. Array Gain

The broadside beamforming analysis applied to the linear array generates artificial spectral density gain. As a result, an array gain formula is applied to the beamformed results to correct the inflated values. The array gain formula presented here is adapted from [16], such that

$$AG = 20 \log l. \quad (30)$$

The array gain correction is performed by subtracting the result of (30) from the calculated array power spectral density.

### 158 H. Algorithm Assessment

(18) and (19) are used to consolidate all channel signals into one array signal. The coherent array spectral critical frequencies are compared to the critical frequencies of a single hydrophone (spectral and coherence) to critically evaluate the performance of the beamformed array.

## 162 IV. RESULTS

### 163 A. Spectral Density

Signal levels (Fig. 2) are relatively high in fast flowing water and low in slow flowing water. The mid-to-high-frequency band is less affected by flow noise and is quiet relative to lower frequencies (< 10 Hz). Evidently, flow noise is prevalent below 100 Hz.

167 The hydrophone power spectrum contains multiple episodes of mid-frequency noise. These signals are  
 168 attributed to ship noise generated by the small vessel used in the ~~gu~~<sup>buoy</sup> drifter tests. Additionally,  
 169 the abrupt shift in spectral densities at  $\sim 90$  minutes is due to equipment reconfigurations.

170 *B. Power Spectrum Probability Density*

171 The PSPD facilitates the broad-scale assessment of a hydrophone's spectral density over entire deploy-  
 172 ment periods. The PSPD for channel 0 is shown in Fig. 3.

173 The PSPD follows a spectral slope of  $f^{-5/3}$  below 10 Hz, behaviour analogous to Kolmogorov's  
 174 turbulence theory. This spectral slope marks a region of flow noise within the signal. A steepened spectral  
 175 slope of  $f^{-m}$ , where  $m > \frac{5}{3}$ , persists between 10 and 100 Hz, a result of small-scale turbulence when  
 176 turbulence wavelength  $<<$  sensor size. This small-scale turbulence is averaged out over the surface of  
 177 the hydrophone sensor, dampening the measured signals. The PSPD results show that ambient noise is  
 178 dominant above 300 Hz, where signal levels are markedly low. Early in the deployment (around 10  
 179 minutes) electronic noise in the system raised the noise floor to 90 dB  $\mu\text{Pa}$ , but this was quickly remedied  
 180 on site. However, an electronic system noise floor persisted at about 60 dB re  $\mu\text{Pa}$ .

181 Single power spectra are superimposed on the PSPD and suggest that measurements in slow current  
 182 conditions contain a greater extent of ambient noise relative to those in fast current conditions.

183 *C. Spectral Critical Frequency*

184 (6) was used to iteratively calculate the spectral slope between 10 and 100 Hz. The linear relationship  
 185 between spectral slope,  $f^{-m}$ , and current,  $u$ , (Fig. 4) indicates that signals recorded in decreasing flow  
 186 are increasingly damped (steepened slope). The inverse relationship between current speed and spectral  
 187 slope suggests that signals are less damped in fast flowing water, a result of larger turbulence scales.  
 188 The spectral slopes observed between 10 and 100 Hz range from -25 to -60 dB/decade. The correlation  
 189 coefficient,  $R$ , suggests that there is a meaningful correlation between spectral slope and current.

190 The spectral critical frequency was iteratively calculated over the experimental period using (7). These  
 191 critical frequencies were regressed against current, as shown in Fig. 5. There is a positive correlation  
 192 between spectral critical frequency and current speed, where fast flow coincides with high spectral critical  
 193 frequencies. As such, the spectral critical frequency is used to track the transition from the flow noise  
 194 region to the ambient noise region.

195 Importantly, the intercepts have not been forced to zero. This is because it is unrealistic to expect that  
196 we can completely eliminate flow noise, or low-frequency noise generated by the mechanical systems that  
197 comprise the tow body. If this were a moored system with no surface expression, that assumption might  
198 be valid, but is not considered here.

199 *D. Spatial Coherence*

200 Spatial coherence is calculated for different hydrophone combinations across the linear array using (3).  
201 The spatial coherence results are presented in magnitude coherence for the entire deployment period (Fig.  
202 6). If the wavelength of propagating sound is sufficiently long, sensors would become relatively co-  
203 located and the coherence would tend to unity. However, the results suggest that the low frequency data  
204 is overwhelmingly incoherent, since the locally generated flow noise is incoherent from one hydrophone  
205 to the next.

206 Flow noise is uncorrelated and propagating ambient noise is highly correlated at low frequencies. As  
207 a result, low coherence and high coherence are a sign of flow noise and ambient noise, respectively.  
208 Therefore, the spatial coherence results are partitioned into two distinct regions: a flow noise region  
209 and an ambient noise region. Visual assessment suggests that flow noise is consistently present at low  
210 frequencies and can be prominent at higher frequencies (above 600 Hz). The ambient noise region is  
211 present between 200 and 600 Hz and contains the same vessel noise identified in Fig. 2.

212 *E. Coherence Critical Frequency*

213 The coherence critical frequency is the frequency at which the boundary between the ambient noise and  
214 flow noise regions occurs. The coherence critical frequency was iteratively calculated for each combination  
215 of channels, and is used to quantify the relative prevalence of flow noise and ambient noise within  
216 a measurement (Fig. 7). The coherence critical frequency is a more rigorous method of flow noise  
217 measurement than the spectral critical frequency, as spatial coherence is an indicator of flow noise cessation  
218 rather than noise region transition. The coherence critical frequency increases with increasing flow speed,  
219 a relationship similar to that of the spectral critical frequency.

220 It is important to note that the coherence is impacted by any temporary deterministic noises present in  
221 the sound field, such as the auxiliary RHIB, mechanical array noise, or noise generated aboard the *MV*  
222 *Nova Endeavour*. In such instances, the automated coherence critical frequency detector fails, and yields  
223 an outlier.

224 There is a good deal of noise in Fig. 7, as no outliers nor oddities were discarded. The retention of  
 225 outliers is done to maintain the integrity of the linear regression. This makes the regression statistically  
 226 rigorous and suggests that the correlation is meaningful.

227 *F. Beamforming*

228 The spectral critical frequency of the beamformed array output can be compared to the single hy-  
 229 drophone spectral and coherence critical frequencies, as shown in Fig. 8. The standard deviations of the  
 230 spectral slope and spatial coherence critical frequency regressions were extracted from the averaged fits,  
 231 while the standard deviation of the coherent array critical frequency regression was calculated from the  
 232 data during the regression.

233 The coherence critical frequencies are relatively high, while spectral critical frequencies (both single  
 234 hydrophone and beamformed array) are relatively low. This is attributed to the more sensitive nature of  
 235 the coherence-based method. Above coherence critical frequencies we can be confident that there is no  
 236 contamination of the ambient noise field by flow noise. Conversely, the single hydrophone and coherent  
 237 array thresholds show where flow noise is dominant. The coherence and spectral critical frequencies  
 238 serve as the respective upper and lower bounds of different noise regimes. Importantly, the coherent array  
 239 contains significantly lower critical frequencies than the single hydrophone, indicating that the broadside  
 240 beamforming approach lessens the extent of flow noise on the measurements.

241 Fig. 9 compares guardbuoy, single hydrophone, and coherent array power spectra at 1.5 hours into the  
 242 experiment. We select a time where the drifter and array were in close proximity to establish a meaningful  
 243 comparison.

244 The GuardBuoy spectrum behaves differently from the rest, exhibiting significantly lower levels at  
 245 frequencies below 100 Hz. A pronounced excursion in spectral slope is present at 10 Hz in the GuardBuoy  
 246 spectrum, suggesting non-negligible flow noise is affecting the drifter's measurements. This is typical of  
 247 all moored or free drifting passive acoustic systems that have a surface expression or subsurface float.  
 248 The single hydrophone shows clear symptoms of flow noise at low frequencies.

249 The spectra reveal that the coherent array spectra transition to the ambient noise region at lower  
 250 frequencies than the single hydrophone. Furthermore, the array signals are quieter than the single hy-  
 251 drophone signals at low frequencies. There is reasonable agreement between the GuardBuoy and coherent  
 252 array above the critical frequency, with some difference above 700 Hz. This disparity is attributed to the

253 lack of co-location between the array and the GuardBuoy, as they are vertically and horizontally displaced  
254 relative to each other.

255 **V. DISCUSSION**

256 *A. Spectral Critical Frequency*

257 Results show that critical frequency and flow speed are positively related, giving the intuitive result that  
258 flow noise is increasingly prevalent in fast current conditions. The spectral critical frequency presents a  
259 method of identifying flow noise prevalence within a signal.

260 The nature of spectral critical frequencies provides two important insights. Firstly, frequencies above  
261 the critical frequency will contain a mixture of ambient noise and flow noise, since the threshold merely  
262 marks the reduction in flow noise, and not the absence. Secondly, frequencies below the critical frequency  
263 will exclusively contain flow noise, since the spectral slopes align with turbulence theory. These insights  
264 are important, as they provide useful context for future signal level and sound-source evaluations in tidal  
265 channel measurements.

266 *B. Spatial Coherence*

267 Spatial coherence results for different sensor combinations show that there are two distinct coherence  
268 regions across the array: an incoherent flow noise region and a coherent ambient noise region. The  
269 prevalence of these regions is quantified with the coherence critical frequency. Iterative calculations of the  
270 coherence critical frequency were regressed against current speed. There is a positive relationship between  
271 coherence critical frequency and current speed. The coherence critical frequency marks the frequency above  
272 which flow noise is absent.

273 The spectral critical frequency provides a lower boundary, below which only flow noise exists, and  
274 the coherence critical frequency method provides an upper boundary, above which only ambient noise  
275 exists. Intermediate frequencies contain a mixture of flow noise and ambient noise. This explains why the  
276 coherence critical frequencies are noticeably higher than those of the spectral method. The application of  
277 spectral and coherence critical frequencies provides valuable insight on the relative extent of both ambient  
278 noise and flow noise within a signal.

279 *C. Beamforming*

280 By effectively treating the array as one sensor or hydrophone, signal processing can address the pseudo-  
 281 sound within low frequency data. Coherent averaging suppresses flow noise and enhances the detection of  
 282 propagating ambient noise. The coherent averaging employs a broadside approach with no steering angle,  
 283 and is outlined in (19).

284 The results of the beamformed array are shown in Fig. 8. Evidently, the coherent array contains lower  
 285 levels and lower critical frequencies than the single hydrophone (Fig. 9). This implies that the coherent  
 286 array is less affected by flow noise, and contains a greater extent of ambient noise.

## 287 VI. CONCLUSION

288 Flow noise appears in two regions: as  $f^{-5/3}$  noise when wavelength  $\gg$  sensor size, and as  $f^{-m}$ , where  
 289 the sensor's finite dimension reduces the flow noise at relatively higher frequencies.  $f^{-m}$  is related to the  
 290 flow speed over the array. A spectrum's deviation from  $f^{-m}$  slope indicates where flow noise is no longer  
 291 dominant. Spatial coherence can be used to identify when the effect of flow noise is negligible.

292 Coherent processing (beamforming) suppresses flow noise and yields a lower spectral critical frequency  
 293 at all flow speeds than that of a single hydrophone. An increased number of hydrophones and array length  
 294 could improve array performance, allowing passive acoustic monitoring at arbitrarily low frequencies.

## 295 REFERENCES

- 296 [1] R. Karsten, A. Swan, and J. Culina, "Assessment of arrays of in-stream tidal turbines in the bay of fundy," *Phil. Trans. R. Soc. A*, vol.  
 297 371, no. 1985, p. 20120189, 2013.
- 298 [2] R. Inger, M. J. Attrill, S. Bearhop, A. C. Broderick, W. James Grecian, D. J. Hodgson, C. Mills, E. Sheehan, S. C. Votier, M. J. Witt  
 299 *et al.*, "Marine renewable energy: potential benefits to biodiversity? an urgent call for research," *Journal of Applied Ecology*, vol. 46,  
 300 no. 6, pp. 1145–1153, 2009.
- 301 [3] M. J. Dadswell, "Occurrence and migration of fishes in minas passage and their potential for tidal turbine interaction," 2010.
- 302 [4] A. Redden and M. Stokesbury, "Acoustic tracking of fish movements in the minas passage and force demonstration area: Pre-turbine  
 303 baseline studies (2011-2013)."
- 304 [5] D. Wang, M. Atlar, and R. Sampson, "An experimental investigation on cavitation, noise, and slipstream characteristics of ocean stream  
 305 turbines," *Proceedings of the Institution of Mechanical Engineers, Part A: Journal of Power and Energy*, vol. 221, no. 2, pp. 219–231,  
 306 2007.
- 307 [6] A. Lombardi, "Soundscape characterization in grand passage, nova scotia, a planned in-stream tidal energy site," 2016.
- 308 [7] M. K. Pine, A. G. Jeffs, and C. A. Radford, "Turbine sound may influence the metamorphosis behaviour of estuarine crab megalopae,"  
 309 *PLoS One*, vol. 7, no. 12, p. e51790, 2012.

- 310 [8] M. Halvorsen, T. Carlson, and A. Copping, "Effects of tidal turbine noise on fish," *PNNL Report-20787 for US Dept of Energy*, WA,  
311 *DC: by Pacific Northwest National Laboratory, Sequim, WA*, pp. 1–41, 2011.
- 312 [9] M. Lighthill, "The bakerian lecture, 1961. sound generated aerodynamically," in *Proceedings of the Royal Society of London A: Mathematical, Physical and Engineering Sciences*, vol. 267, no. 1329. The Royal Society, 1962, pp. 147–182.
- 313 [10] M. Strasberg, "Nonacoustic noise interference in measurements of infrasonic ambient noise," *The Journal of the Acoustical Society of America*, vol. 66, no. 5, pp. 1487–1493, 1979.
- 314 [11] M. Van Dyke, *An album of fluid motion*. Parabolic Press Stanford, 1982, vol. 176.
- 315 [12] C. Bassett, J. Thomson, P. H. Dahl, and B. Polagye, "Flow-noise and turbulence in two tidal channels," *The Journal of the Acoustical Society of America*, vol. 135, no. 4, pp. 1764–1774, 2014.
- 316 [13] V. O. Knudsen, R. Alford, and J. Emling, "Underwater ambient noise," *J. Mar. Res.*, vol. 7, pp. 410–429, 1948.
- 317 [14] D. R. Barclay and M. J. Buckingham, "Depth dependence of wind-driven, broadband ambient noise in the philippine sea," *The Journal of the Acoustical Society of America*, vol. 133, no. 1, pp. 62–71, 2013.
- 318 [15] N. D. Merchant, T. R. Barton, P. M. Thompson, E. Pirotta, D. T. Dakin, and J. Dorocicz, "Spectral probability density as a tool for ambient noise analysis," *The Journal of the Acoustical Society of America*, vol. 133, no. 4, pp. EL262–EL267, 2013.
- 319 [16] H. Cox, "Line array performance when the signal coherence is spatially dependent," *The Journal of the Acoustical Society of America*,  
320 vol. 54, no. 6, pp. 1743–1746, 1973.
- 321

322 326 **Michael Shell** Biography text here.

PLACE  
PHOTO  
HERE

327

328 **John Doe** Biography text here.

329 **Jane Doe** Biography text here.

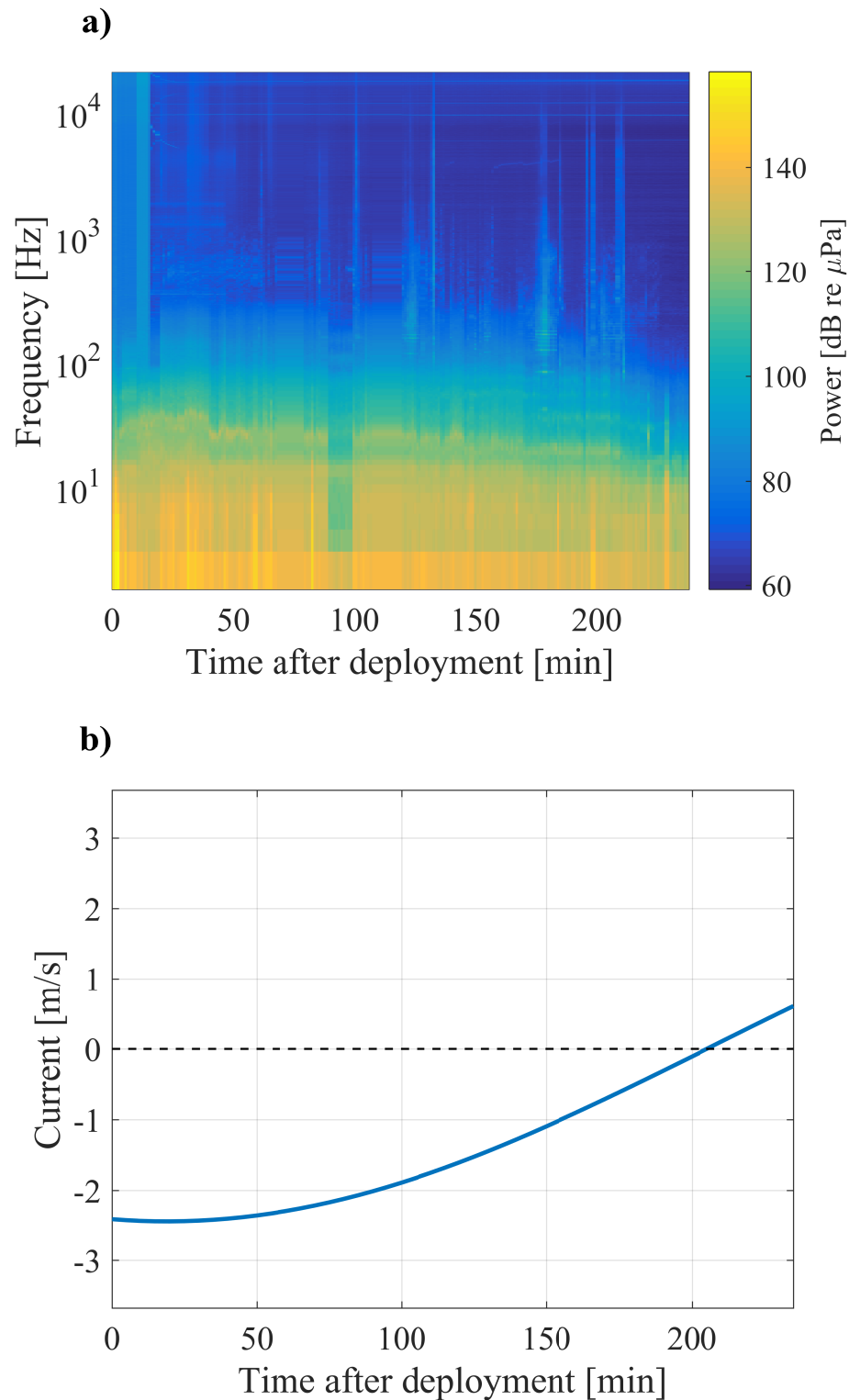


Fig. 2. Power spectrum for channel 0 on the array (a). The spectrum is plotted over the deployment period across a range of low-to-mid frequencies. The spectrum begins at maximum ebb tide and ends at slack tide, as shown by the current time series (b). Power decreases with flow speed over the deployment period.

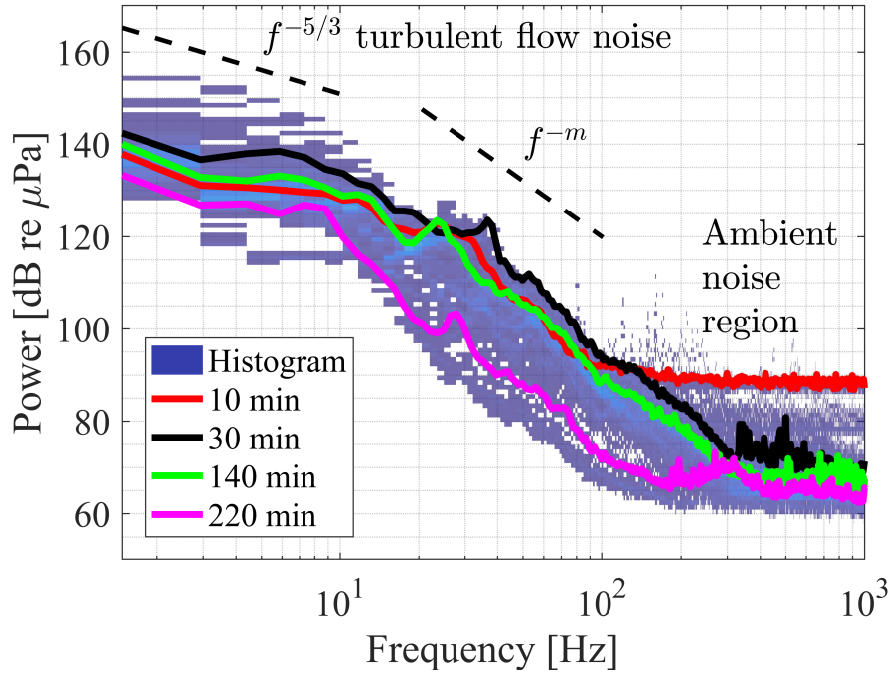


Fig. 3. Channel 0 power spectrum probability density over the entire deployment period. Turbulent flow noise is prevalent  $< 10$  Hz (where wavelengths  $\gg$  sensor size), with a spectral slope of  $f^{-5/3}$ , while turbulence interacting with the hydrophone's finite size (in the 10 Hz to 100 Hz band) yields a spectral slope of  $f^{-m}$ . The ambient sound field dominates at  $< 300$  Hz. Time indicates the single spectra time stamp.

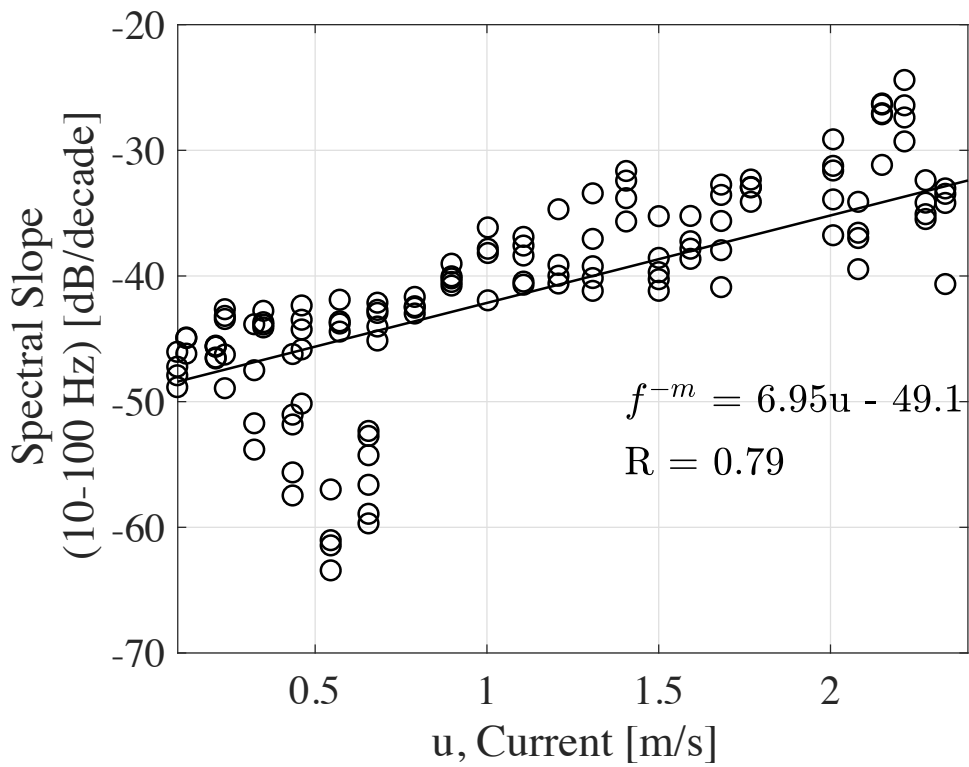


Fig. 4. Relationship between spectral slope,  $f^{-m}$ , and current,  $u$ , between 10 and 100 Hz for channel 0. Spectral slope magnitude increases with decreasing flow. Spectral slopes are steeper than Knudsen's -17 dB./decade. Correlation coefficients,  $R$ , are reported.

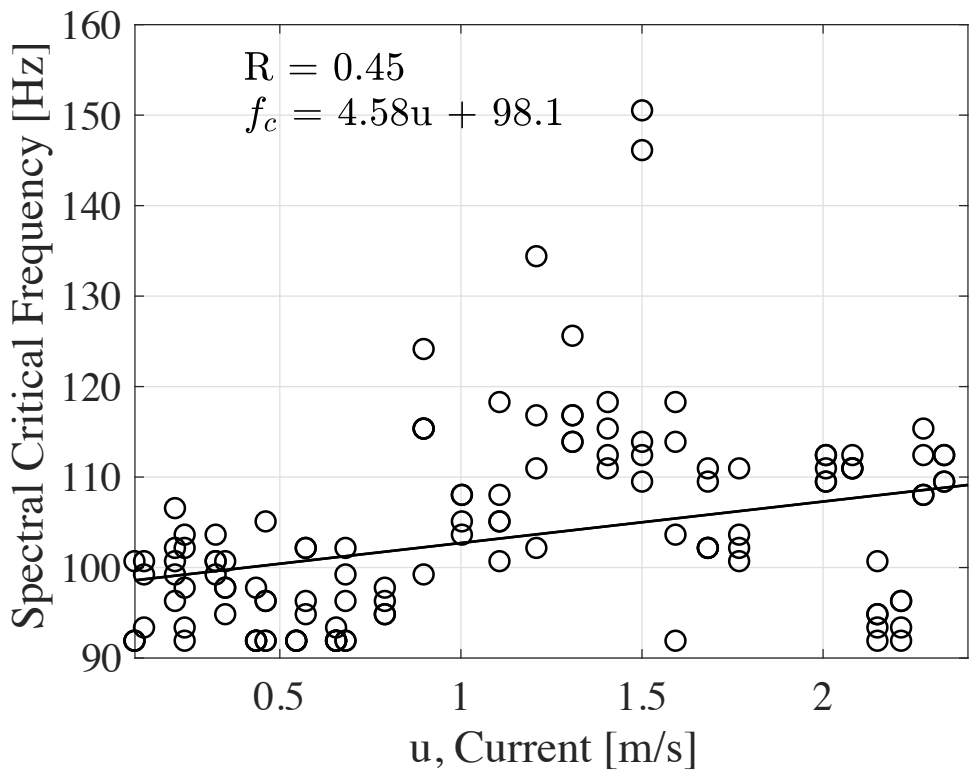


Fig. 5. Relationship between spectral critical frequency,  $f_c$ , and current,  $u$ , for channel 0. Spectral critical frequency reveals where flow noise is no longer dominant. Correlation coefficients,  $R$ , are reported.

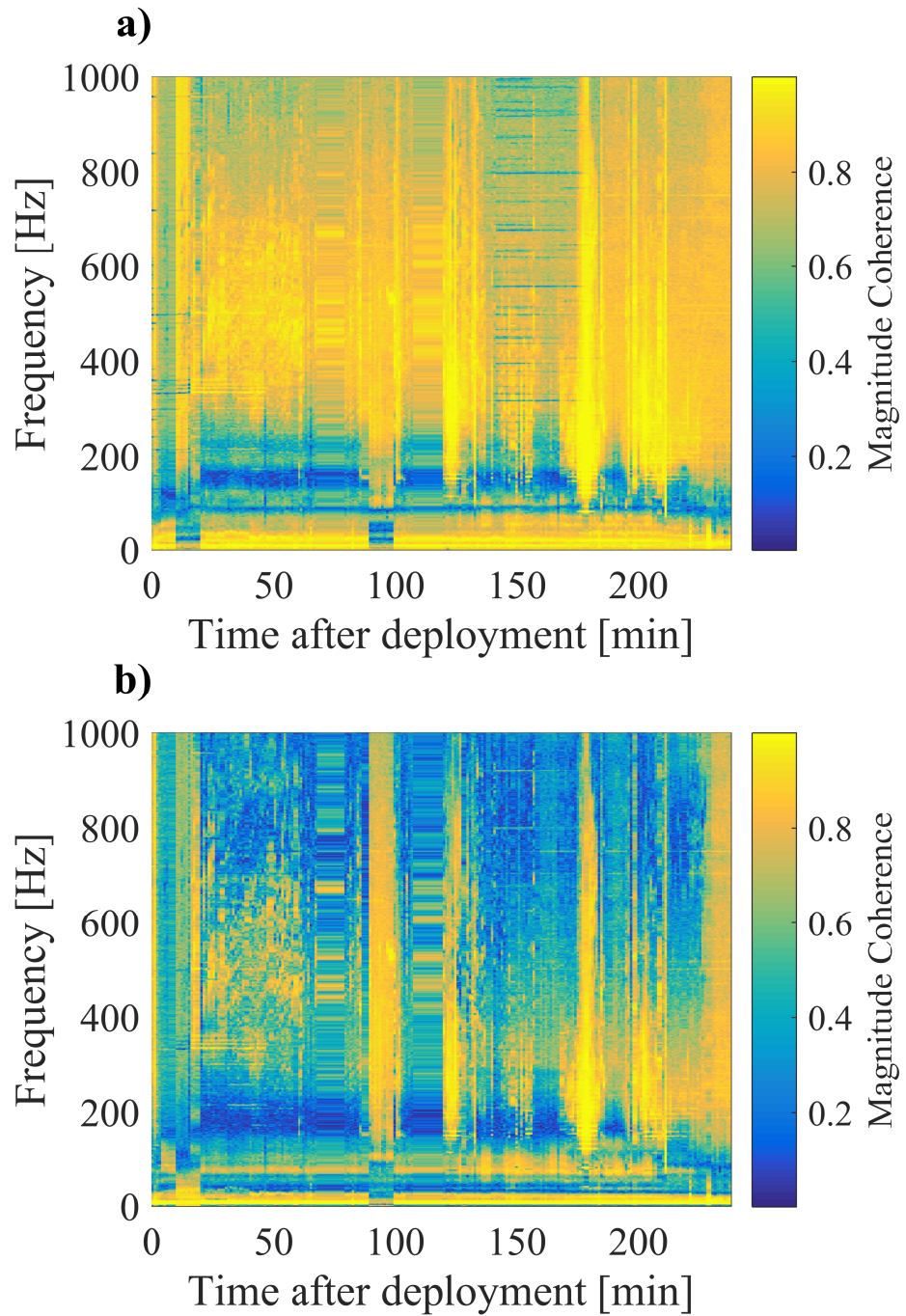


Fig. 6. Spatial coherence over the experimental period. Magnitude coherence is expected to tend to unity as the hydrophones become relatively co-located. However, uncorrelated flow noise on each phone breaks that relationship. Incoherent flow noise regions increase with current speed. Channel 0 - 1 (a) and 0 - 3 (b) are shown as examples. Results hold to all other channel combinations.

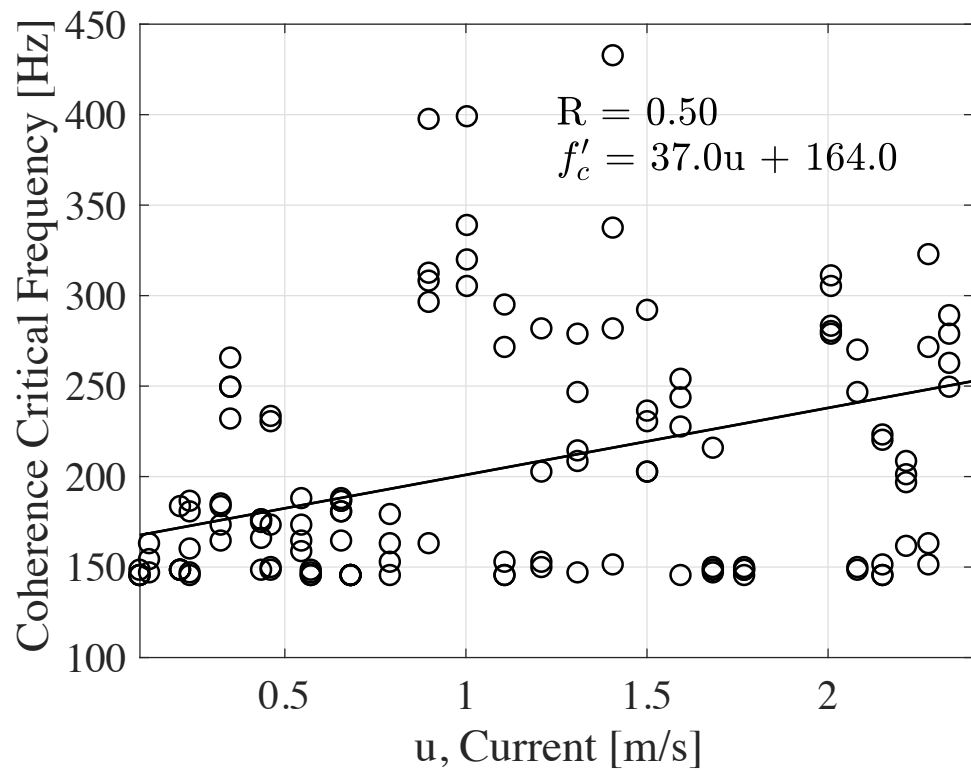


Fig. 7. Relationship between coherence critical frequency,  $f'_c$ , and current,  $u$ , for channels 0 - 1. Coherence critical frequency is used to detect the critical frequency in a more precise way than the spectral approach.

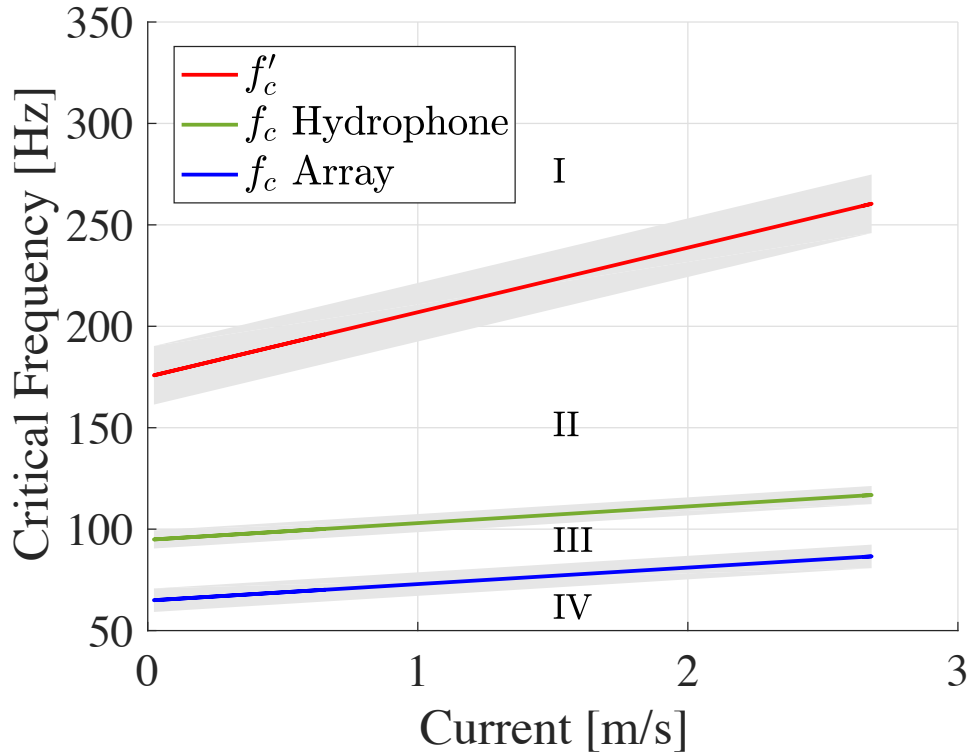


Fig. 8. Comparison of hydrophone spectral critical frequency, coherence critical frequency, and array spectral critical frequency distributions. Coherence and spectral critical frequencies reveal regions of flow noise, ambient noise, and a mixture of both. Uncertainties are one standard deviation (shaded). I is an ambient noise region, II is a region of ambient noise and flow noise, III is a region of flow noise measured on a single hydrophone, and IV is a region of flow noise measured on the coherent array.

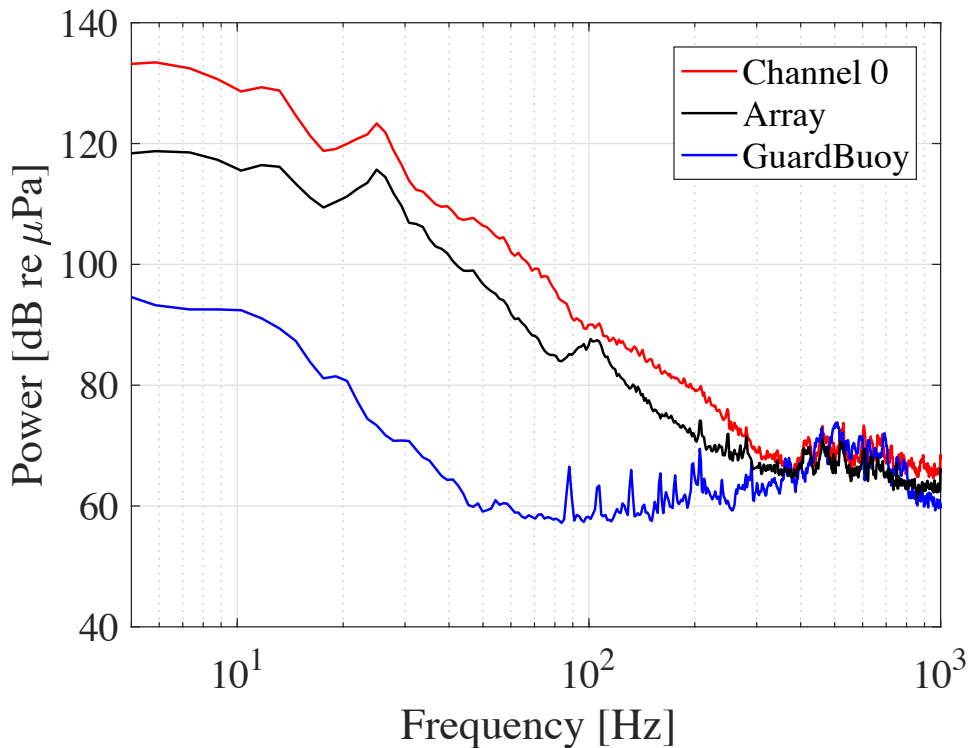


Fig. 9. Comparison of channel 0 (single hydrophone), coherent array, and GuardBuoy power spectra at 1.5 hr into the deployment.